Astronomy
&
Astrophysics

Pulsating low-mass white dwarfs in the frame of new evolutionary sequences

III. The pre-ELM white dwarf instability strip

A. H. Córsico[1,2], L. G. Althaus[1,2], A. M. Serenelli[3], S. O. Kepler[4], C. S. Jeffery[5], and M. A. Corti[1,6]

[1] Grupo de Evolución Estelar y Pulsaciones, Facultad de Ciencias Astronómicas y Geofísicas, Universidad Nacional de La Plata, Paseo del Bosque s/n, 1900 La Plata, Argentina
e-mail: `acorsico,althaus@fcaglp.unlp.edu.ar`
[2] Instituto de Astrofísica La Plata, CONICET-UNLP, Paseo del Bosque s/n, 1900 La Plata, Argentina
[3] Instituto de Ciencias del Espacio (ICE-CSIC/IEEC) Campus UAB, Carrer de Can Magrans, s/n 08193 Cerdanyola del Vallés, Spain
[4] Departamento de Astronomia, Universidade Federal do Rio Grande do Sul, Av. Bento Goncalves 9500, 91501-970 Porto Alegre, RS, Brazil
[5] Armagh Observatory, College Hill, Armagh BT61 9DG, UK
[6] Instituto Argentino de Radioastronomía, CCT-La Plata, CONICET, C.C. Nro. 5, 1984 Villa Elisa, Argentina

ABSTRACT

Context. Many low-mass ($M_\star/M_\odot \lesssim 0.45$) and extremely low-mass (ELM, $M_\star/M_\odot \lesssim 0.18-0.20$) white-dwarf stars are currently being found in the field of the Milky Way. Some of these stars exhibit long-period gravity-mode (*g*-mode) pulsations, and constitute the class of pulsating white dwarfs called ELMV stars. In addition, two low-mass pre-white dwarfs, which could be precursors of ELM white dwarfs, have been observed to show multiperiodic photometric variations. They could constitute a new class of pulsating low-mass pre-white dwarf stars.
Aims. Motivated by this finding, we present a detailed nonadiabatic pulsation study of such stars, employing full evolutionary sequences of low-mass He-core pre-white dwarf models.
Methods. Our pulsation stability analysis is based on a set of low-mass He-core pre-white dwarf models with masses ranging from 0.1554 to 0.2724 $M_\odot$, which were derived by computing the nonconservative evolution of a binary system consisting of an initially 1 $M_\odot$ ZAMS star and a 1.4 $M_\odot$ neutron star companion. We have considered models in which element diffusion is accounted for and also models in which it is neglected.
Results. We confirm and explore in detail a new instability strip in the domain of low gravities and low effective temperatures of the $T_{\rm eff} - \log g$ diagram, where low-mass pre-white dwarfs are currently found. The destabilized modes are radial and nonradial *p* and *g* modes excited by the $\kappa - \gamma$ mechanism acting mainly at the zone of the second partial ionization of He, with non-negligible contributions from the region of the first partial ionization of He and the partial ionization of H. The computations with element diffusion are unable to explain the pulsations observed in the two known pulsating pre-white dwarfs, suggesting that element diffusion might be inhibited at these stages of the pre-white dwarf evolution. Our nonadiabatic models without diffusion, on the other hand, naturally explain the existence and range of periods of the pulsating pre-white dwarf star WASP J1628+10B, although they fail to explain the pulsations of WASP J0247−25B, the other known member of the class, indicating that the He abundance in the driving region of this star might be substantially higher than predicted by our models.
Conclusions. Discoveries of additional members of this new class of pulsating stars and their analysis in the context of the theoretical background presented in this paper will shed new light on the evolutionary history of their progenitor stars.

Key words. asteroseismology – stars: oscillations – stars: evolution – stars: interiors – white dwarfs

1. Introduction

Most of the low- and intermediate-mass stars that populate our Universe, including our Sun, will become white dwarf (WD) stars at the very late stages of their lives (Winget & Kepler 2008; Fontaine & Brassard 2008; Althaus et al. 2010). The majority of WDs show H-rich atmospheres, which define the spectral class of DA WDs. While most of DA WDs have a mass near ~0.60 $M_\odot$ (Kepler et al. 2007, 2015; Tremblay et al. 2011; Kleinman et al. 2013) and harbor C/O cores, there is a low-mass tail of the mass distribution corresponding to objects with $M_\star/M_\odot \lesssim 0.45$,

which likely have cores made of He[1]. These low-mass WD stars are thought to be the outcome of strong mass-loss events at the red giant branch stage of low-mass stars in binary systems before the He flash that, in this way, is avoided (Althaus et al. 2010). In particular, binary evolution is the most likely origin for the so-called extremely low-mass (ELM) WDs, which have masses below ~0.18−0.20 $M_\odot$ (see the recent theoretical studies

---

[1] There is another component of the WD mass distribution, corresponding to high-mass WDs ($M_\star/M_\odot \gtrsim 1.0$), with cores probably composed of C and O or O, Mg, and Ne.

by Althaus et al. 2013; Istrate et al. 2014). As has been known for a long time (e.g., Driebe et al. 1998), models predict that ELM WDs harbor very thick H envelopes able to sustain residual H nuclear burning via pp-chain, leading to markedly long evolutionary timescales.

An increasing number of low-mass WDs, including ELM WDs, are being detected through the ELM survey and the SPY and WASP surveys (Koester et al. 2009; Brown et al. 2010, 2012, 2013; Maxted et al. 2011; Kilic et al. 2011, 2012, 2015; Gianninas et al. 2014, 2015). While these stars are already extremely exciting in their own right, the interest in them has been strongly intensified because some of them pulsate in nonradial g (gravity) modes (ELMVs, Hermes et al. 2012, 2013b,a; Kilic et al. 2015; Bell et al. 2015). This constitutes an unprecedented opportunity for probing their interiors and eventually to test their formation channels by employing the tools of asteroseismology. Theoretical adiabatic pulsational analysis of these stars carried out by Steinfadt et al. (2010), Córsico et al. (2012), Córsico & Althaus (2014a) show that g modes in ELM WDs are restricted mainly to the core regions, providing the chance to constrain the core chemical structure. Also, nonadiabatic stability computations reveal that many unstable g and p modes are excited by a combination of the $\kappa - \gamma$ mechanism (Unno et al. 1989) and the "convective driving" mechanism (Brickhill 1991), both of them acting at the H-ionization zone (Córsico et al. 2012; Van Grootel et al. 2013; Córsico & Althaus 2016), and that some unstable short period g modes can be driven by the ε mechanism due to stable H burning (Córsico & Althaus 2014b).

High-frequency pulsations in a precursor of a low-mass WD star component of an eclipsing binary system were reported for the first time by Maxted et al. (2013). This object, previously discovered by Maxted et al. (2011), is named 1SWASP J024743.37−251549.2B (hereinafter WASP J0247−25B). Its parameters are $T_{\rm eff} = 11\,380 \pm 400$ K, $\log g = 4.576 \pm 0.011$, and $M_\star = 0.186\,M_\odot$, as given by Maxted et al. (2013). It shows variability with periods (Π) in the range 380−420 s, supposed to be due to a mixture of radial ($\ell = 0$) and nonradial ($\ell \geq 1$) p modes (Maxted et al. 2013). Evolutionary models predict that this star is evolving to higher effective temperatures at nearly constant luminosity prior to becoming a low-mass WD. This star could be the first member of a new class of pulsating stars that are the precursors of low-mass (including ELM) WDs. A second star of this type, 1SWASP J162842.31+101416.7B (hereinafter WASP J1628+10B, $T_{\rm eff} = 9200 \pm 600$ K, $\log g = 4.49 \pm 0.05$, $M_\star = 0.135\,M_\odot$) was discovered by Maxted et al. (2014) in another eclipsing binary system, showing high-frequency signals with periods in the range 668−755 s, likely to be due to pulsations similar to those seen in WASP J0247−25B. The study of Jeffery & Saio (2013) constitutes the only theoretical work exploring the pulsation stability properties of radial modes of low-mass He-core pre-WD models considering a range of envelope chemical compositions, effective temperatures and luminosities. On the basis of a huge set of static envelope models, Jeffery & Saio (2013) were successful to identify the instability boundaries associated with radial modes characterized by low-to-high radial orders, and showed that they are very sensitive to the chemical composition at the driving region. These authors found that the excitation of modes is by the $\kappa - \gamma$ mechanism operating mainly in the second He ionization zone, provided that the driving region is depleted in H ($0.2 \lesssim X_{\rm H} \lesssim 0.3$).

In this paper, the third work of a series devoted to low-mass WD stars, we carry out a detailed radial and nonradial stability analysis on a set of He-core, low-mass pre-WD evolutionary models extracted from the computations of Althaus et al. (2013).

At variance with the study of Jeffery & Saio (2013), who employ static envelope models, we use here fully evolutionary models that represent the precursors of low-mass and ELM WDs. The use of homogeneous envelope models by Jeffery & Saio (2013) enables to primarily establish where pulsational instability might occur in the HR diagram, and allows for a full exploration of how the pulsational instabilities are affected when parameters such as the stellar mass and the chemical composition at the driving regions (in the stellar envelope) are varied. The use of evolutionary models, on the other hand, involves time-dependent evolution processes that can have a strong impact on the chemical structure at the driving regions (for instance, element diffusion). Also, in addition to determine the instability domains and the ranges of excited periods, the employment of complete evolutionary models makes it possible to test the theories of formation of these stars, that is, the progenitor evolution. Ultimately, both approaches – static and evolutionary models – are complementary.

The paper is organized as follows. In Sect. 2 we briefly describe our numerical tools and the main ingredients of the evolutionary sequences we employ to assess the nonadiabatic pulsation properties of low-mass He-core pre-WDs. In Sect. 3 we present our pulsation results in detail, devoting Sect. 3.1 to present our nondiffusion computations, and Sect. 3.2 to show the results for the case in which element diffusion is allowed to operate. In Sect. 4 we compare the predictions of our nonadiabatic models with the observed stars. Finally, in Sect. 5 we summarize the main findings of the paper.

2. Modelling

2.1. Numerical codes

The pulsational analysis presented in this work makes use of full stellar evolution models of pre-WDs generated with the LPCODE stellar evolution code. LPCODE computes in detail the complete evolutionary stages leading to WD formation, allowing the WD and pre-WD evolution to be studied in a consistent way based on the evolutionary history of progenitors. Details of LPCODE can be found in Althaus et al. (2005, 2009, 2013) and references therein. Here, we mention only those ingredients employed which are relevant for our analysis of low-mass, He-core WD and pre-WD stars (see Althaus et al. 2013, for details). The standard Mixing Length Theory (MLT) for convection in the version ML2 is used (Tassoul et al. 1990). In this prescription, due to Bohm & Cassinelli (1971), the parameter α (the mixing length in units of the local pressure scale height) is set equal to 1, while the coefficients a, b, c that appear in the equations for the average speed of the convective cell, the average convective flux, and the convective efficiency (see Cox 1968), have values $a = 1, b = 2, c = 16$. We emphasize that the results presented in this work are insensitive to the prescription of the MLT employed. In particular, we have also used the ML1 ($\alpha = 1, a = 1/8, b = 1/2, c = 24$, Böhm-Vitense 1958) and ML3 ($\alpha = 2, a = 1, b = 2, c = 16$, Tassoul et al. 1990) recipes, and we obtain the same results than for ML2. The metallicity of the progenitor stars has been assumed to be $Z = 0.01$. It is worth mentioning that the pulsation stability results presented in this paper do not depend on the value of Z[2]. Radiative opacities for arbitrary metallicity in the range from 0

---

[2] The value of Z only has a moderate impact on the value of the theoretical mass threshold for the development of CNO flashes (Sarna et al. 2000), which in the frame of our evolutionary models is ~0.18 $M_\odot$ (Althaus et al. 2013). Panei et al. (2007) assume $Z = 0.02$ for the progenitor stars and obtain a value of ~0.17 $M_\odot$ for the mass threshold.

to 0.1 are from the OPAL project (Iglesias & Rogers 1996). Conductive opacities are those of Cassisi et al. (2007). The equation of state during the main sequence evolution is that of OPAL for H- and He-rich compositions. Neutrino emission rates for pair, photo, and bremsstrahlung processes have been taken from Itoh et al. (1996), and for plasma processes we included the treatment of Haft et al. (1994). For the WD regime we have employed an updated version of the Magni & Mazzitelli (1979) equation of state. The nuclear network takes into account 16 elements and 34 thermonuclear reaction rates for pp-chains, CNO bi-cycle, He burning, and C ignition. Time-dependent diffusion due to gravitational settling and chemical and thermal diffusion of nuclear species has been taken into account following the multicomponent gas treatment of Burgers (1969). Abundance changes have been computed according to element diffusion, nuclear reactions, and convective mixing. This detailed treatment of abundance changes by different processes during the WD regime constitutes a key aspect in the evaluation of the importance of residual nuclear burning for the cooling of low-mass WDs.

We carry out a pulsation stability analysis of radial ($\ell = 0$) and nonradial ($\ell = 1, 2$) p and g modes employing the nonadiabatic versions of the LP–PUL pulsation code described in detail in Córsico et al. (2006). For the nonradial computations, the code solves the sixth-order complex system of linearized equations and boundary conditions as given by Unno et al. (1989). For the case of radial modes, LP–PUL solves the fourth-order complex system of linearized equations and boundary conditions according to Saio et al. (1983), with the simplifications of Kawaler (1993). Our nonadiabatic computations rely on the frozen-convection (FC) approximation, in which the perturbation of the convective flux is neglected. While this approximation could not be strictly valid in the case of the longest-period g modes considered, we do not expect large variations of the nonadiabatic results if a time-dependent convection treatment is used (TDC; see, for instance, Van Grootel et al. 2013; Saio 2013) instead, although we must keep in mind that this issue can constitute a source of uncertainties in the location of the blue edges of instability computed in this work. The Brunt-Väisälä frequency, N, is computed as in Tassoul et al. (1990). That prescription for the computation of N involves the so called "Ledoux term" B, which is closely related to the chemical gradients in the interior of the WDs and pre-WDs (see Tassoul et al. 1990, for details).

2.2. Model sequences

Althaus et al. (2013) derived realistic configurations for low-mass He-core WDs by mimicking the binary evolution of progenitor stars. Full details of this procedure are given by Althaus et al. (2013). Binary evolution was assumed to be fully nonconservative, and the loss of angular momentum due to mass loss, gravitational wave radiation, and magnetic braking was considered. All of the He-core pre-WD initial models were derived from evolutionary calculations for binary systems consisting of an evolving Main Sequence low-mass component (donor star) of initially 1 $M_\odot$ and a 1.4 $M_\odot$ neutron star companion as the other component. Different masses for the initial donor star could lead to low-mass pre-WD models with different He abundances in their envelopes. A total of 14 initial He-core pre-WD models with stellar masses between 0.1554 and 0.4352 $M_\odot$ were computed for initial orbital periods at the beginning of the Roche lobe phase in the range 0.9 to 300 d. In Table 1, we provide some relevant characteristics of the subset of He-core pre-WD model sequences employed in this work which have masses in the range 0.1554 $\lesssim M_\star/M_\odot \lesssim$ 0.2724. In Althaus et al. (2013),

Table 1. Selected properties of our He-core pre-WD sequences.

$M_\star/M_\odot$	$X_{\rm H}^{\rm surf}$	$M_{\rm H}/M_\odot$ [10^{-3}]	$\tau_{\rm instability}$ [yr]
0.1554	0.365	4.34	1.9×10^9
0.1612	0.376	4.19	1.3×10^9
0.1650	0.390	4.09	1.1×10^9
0.1706	0.405	3.94	4.1×10^8
0.1762	0.423	3.80	2.5×10^8
0.1822	0.440	3.66	1.6×10^8
0.1869	0.453	3.55	1.4×10^8
0.1921	0.466	3.42	5.8×10^7
0.2026	0.490	3.22	6.5×10^7
0.2390	0.701	2.86	3.4×10^7
0.2724	0.715	2.02	–

Notes. The table lists the stellar mass, the H surface abundance, the mass of the H content at the point of maximum $T_{\rm eff}$ at the beginning of the first cooling branch, and the time it takes the models to evolve along the instability domain (thick blue lines in Fig. 1) in the nondiffusion computations.

the complete evolution of these models was computed down to the range of luminosities of cool WDs, including the stages of multiple thermonuclear CNO flashes during the beginning of the cooling branch. In this paper, however, we focus only on the evolutionary stages previous to the WD evolution, that is, *before* the stars reach their maximum effective temperature at the beginning of the first cooling branch. The adiabatic and nonadiabatic pulsation properties on the final cooling branches were already analyzed in our previous works of this series (Córsico & Althaus 2014a, 2016). Column 1 of Table 1 shows the stellar masses ($M_\star/M_\odot$). The second column corresponds to the H surface abundance, while the third column shows the mass of the H content at the point of maximum effective temperature at the beginning of the first cooling branch. Finally, Col. 4 indicates the time spent by models in the instability domain, marked with thick blue lines in Fig. 1.

3. Stability analysis

3.1. Computations neglecting element diffusion

We analyzed the stability pulsation properties of He-core, low-mass pre-WD models computed assuming the ML2 prescription for the MLT theory of convection (see Tassoul et al. 1990) and covering a range of effective temperatures of 25 000 K $\gtrsim T_{\rm eff} \gtrsim$ 6000 K and a range of stellar masses of 0.1554 $\lesssim M_\star/M_\odot \lesssim$ 0.2724. In this section we report on the results of computations in which we assume that element diffusion due to gravitational settling and chemical and thermal diffusion is not operative. That is, it is assumed that each model preserves the outer He/H homogeneous chemical structure resulting from the previous evolution. We defer the case in which time-dependent element diffusion is allowed to operate to Sect. 3.2. For each model, we assessed the pulsational stability of radial ($\ell = 0$), and nonradial ($\ell = 1, 2$) p and g modes with periods in the range 10 s $\lesssim \Pi \lesssim$ 20 000 s. The reason for considering such a wide range of periods in our computations is to clearly define the theoretical domain of instability of pre-ELMV WDs[3], that is, to find

---

[3] For simplicity, here and throughout the paper we refer to the pulsating low-mass pre-WDs as pre-ELMV WDs, even in the cases in which $M_\star \gtrsim 0.18$–$0.20\ M_\odot$.
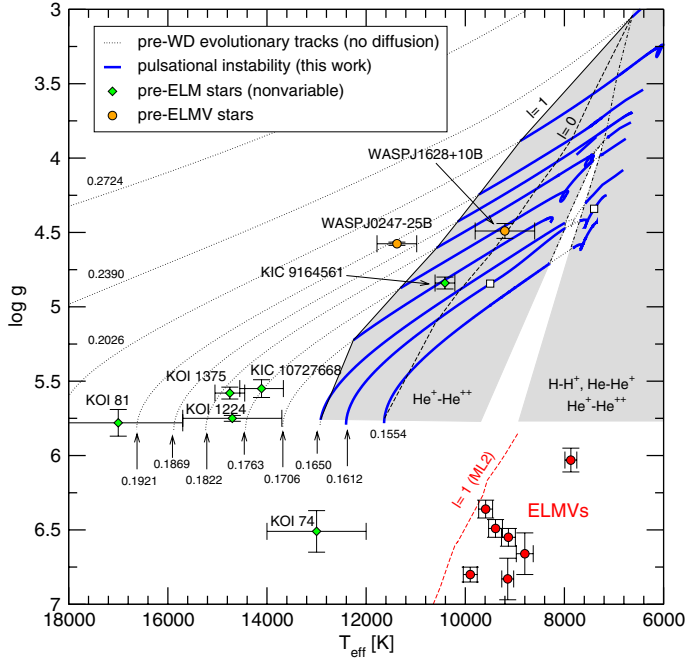
Fig. 1. $T_{\rm eff} - \log g$ diagram showing our low-mass He-core pre-WD evolutionary tracks (dotted curves) computed neglecting element diffusion. Numbers correspond to the stellar mass of each sequence. The locations (with their uncertainties) of the known ELMVs are marked with red dots, along with the theoretical $\ell = 1$ g-mode blue edge (red dashed curve) computed by Córsico & Althaus (2016). Orange dots with error bars correspond to the pre-ELMV stars discovered by Maxted et al. (2013, 2014), and light green diamonds depict the location of pre-ELM (nonvariable) WDs observed in the *Kepler* mission field. The solid black line indicates the nonradial dipole ($\ell = 1$) blue edge of the pre-ELMV instability domain (emphasized as a gray area, which is an extrapolation) due to the $\kappa - \gamma$ mechanism acting at the He$^+$–He^{++} partial ionization region, as obtained in this work. The $\ell = 2$ blue edge (not plotted) is nearly coincident with the $\ell = 1$ blue edge (see Sect. 3.1). Similarly, the dashed black line indicates the blue edge of the instability strip for radial ($\ell = 0$) modes. Stellar models having unstable nonradial modes are emphasized on the evolutionary tracks with thick blue lines. The dot-dashed black lines mark the limits between the instability zones in which the partial ionization of H–H$^+$ and He–He$^+$ does contribute to the driving of modes (right zone) and does not (left zone). The two hollow squares on the evolutionary track of $M_\star = 0.1612$ $M_\odot$ indicate the location of the template models analyzed in Sect. 3.

the long- and short-period edges of the instability domains for all the stellar masses and effective temperatures.

We start by examining Fig. 1, in which we show the location of the $\ell = 1$ blue (hot) edge of the instability domain of our low-mass He-core pre-WD models on the $T_{\rm eff} - \log g$ plane with a solid black line. The blue edge for $\ell = 2$ modes (not shown in the plot) is a little (~10−30 K) hotter than the $\ell = 1$ blue edge. We emphasize that the location of the blue edges does not depend on the prescription for the MLT theory of convection adopted in the equilibrium models. The blue edge of the instability domain associated with radial ($\ell = 0$) modes is depicted with a dashed black line. Visibly, the blue edge for radial modes is substantially cooler than for nonradial modes. The parts of the nondiffusion evolutionary tracks (drawn with dotted thin lines) associated with stellar models having at least one unstable nonradial mode are emphasized with thick blue lines. There is a strong dependence of the blue edges on the stellar mass, i.e., the blue edges are hotter for the less massive model sequences. This mass dependence is connected with the abundance of He at the

driving regions (see later) of the models. We also include in the plot the blue edge of the theoretical $\ell = 1$ ELM WD instability strip (red dashed line) according to Córsico & Althaus (2016), along with the seven ELMVs discovered so far (Hermes et al. 2012, 2013b,a; Kilic et al. 2015; Bell et al. 2015), marked with red dots. In comparison, the slope of the $\ell = 1$ blue edge of the pre-ELMVs is slightly less steep but much hotter than the blue edge of the ELMVs. As a result, the instability domain of pre-ELMVs is substantially more extended in effective temperature. We have also included in Fig. 1 the location of two pulsating pre-WD stars discovered by Maxted et al. (2013, 2014; WASP J0247−25B and WASP J1628+10B, respectively). Finally, we plot the location of six nonvariable low-mass pre-WDs in binary systems with companion A stars, observed in the *Kepler* field. They are KIC 9164561 and KIC 10727668 (Rappaport et al. 2015), KOI 74 and KOI 81 (van Kerkwijk et al. 2010), KOI 1375 (Carter et al. 2011), and KOI 1224 (Breton et al. 2012). Our current computations without element diffusion seems to account only for the pulsations of WASP J1628+10B, but not for WASP J0247−25B. On the other hand, our analysis predicts pulsational instabilities at the effective temperature and gravity of the constant (nonvariable) star KIC 9164561. We will return to this issue in Sect. 4.

3.1.1. Propagation diagrams

Here, we describe the nonradial stability properties of two template 0.1612 $M_\odot$ low-mass He-core pre-WD models with $T_{\rm eff} = 7400$ K and $T_{\rm eff} = 9500$ K[4]. Their locations in the $T_{\rm eff} - \log g$ diagram are displayed in Fig. 1 as two hollow squares in the 0.1612 $M_\odot$ evolutionary track. These properties are representative of all the models of our complete set of evolutionary sequences. In the upper panel of Fig. 2 we display the internal chemical profiles for He and H corresponding to the template model with $T_{\rm eff} \sim 7400$ K. The model is characterized by a core made of pure He surrounded by an envelope with uniform chemical composition of H ($X_{\rm H} = 0.38$) and He ($X_{\rm He} = 0.61$) up to the surface. In addition, we show in the same panel the Ledoux term B (related to the computation of the Brunt-Väisälä frequency; see Tassoul et al. 1990, for its definition), which has nonzero values only at the chemical gradient associated with the He/H transition region.

The He/H chemical transition region leaves notorious signatures in the run of the squared critical frequencies, in particular in the Brunt-Väisälä frequency. This is clearly displayed in the propagation diagram (Cox 1980; Unno et al. 1989) of the lower panel in Fig. 2. g modes propagate in the regions of the star where $\sigma^2 < N^2, L_\ell^2$, and p modes in the regions where $\sigma^2 > N^2, L_\ell^2$. Here, L_ℓ is the Lamb (acoustic) frequency, defined as $L_\ell^2 = \ell(\ell + 1)c_s^2/r^2$ (c_s being the local adiabatic sound speed), and σ is the oscillation frequency. Because of the very peculiar shape of the Brunt-Väisälä frequency in the inner regions of the star, there is a considerable range of intermediate frequencies for which the modes behave like g modes in the inner parts of the star and like p modes in the outer parts. A similar situation is found in hydrogen-deficient pre-WD models representative of PG 1159 stars before the evolutionary knee (see Fig. 6 of Córsico & Althaus 2006). These intermediate-frequency modes are called "mixed modes" (Scuflaire 1974; Osaki 1975; Aizenman et al. 1977). Mixed modes and the associated phenomena of avoided crossing and mode bumping –

---

[4] The stability properties of radial modes are qualitatively similar to those of nonradial modes, and therefore they will not be described.
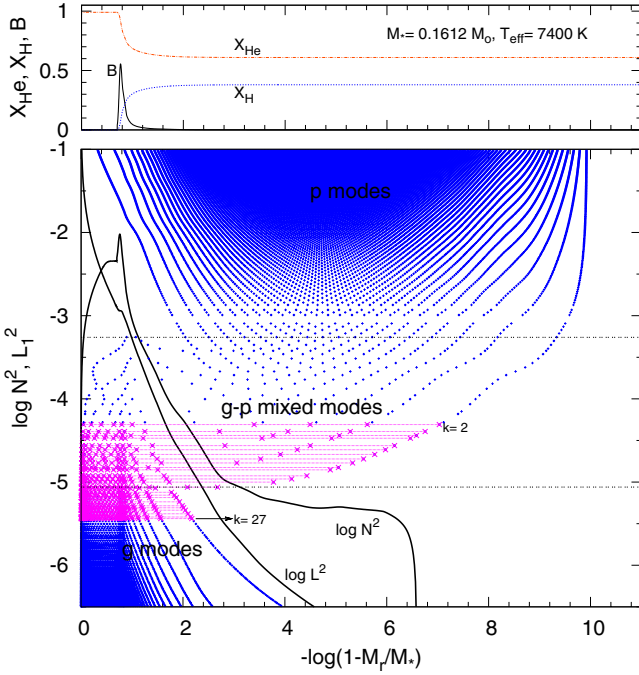
Fig. 2. Internal chemical profiles of He and H and the Ledoux term B (*upper panel*) and the propagation diagram – the run of the logarithm of the squared critical frequencies (N^2, L_ℓ^2) – (*lower panel*), in terms of the outer mass fraction coordinate, corresponding to the pre-WD template model of $M_\star = 0.1612\ M_\odot$ and $T_{\rm eff} \sim 7400$ K marked in Fig. 1. In the lower panel, small "+"symbols (in blue) correspond to the spatial location of the nodes of the radial eigenfunction of dipole ($\ell = 1$) g, p and $g-p$ mixed modes. The (squared) frequency interval corresponding to $g-p$ mixed modes is enclosed with two dotted horizontal lines. Nodes corresponding to unstable modes (from the $k = 2$ g mixed mode to the $k = 27$ pure g mode) are emphasized with "×" symbols (in magenta) connected with thin lines.

Fig. 3. Same as Fig. 2, but for the pre-WD template model of $M_\star = 0.1612\ M_\odot$ and $T_{\rm eff} \sim 9500$ K marked in Fig. 1.

where the periods approach quite closely without actually crossing – have been extensively studied in the context of sub-giants and red giant pulsating stars (see, e.g., Christensen-Dalsgaard & Houdek 2010; Deheuvels & Michel 2010). In the figure, the frequency range of mixed modes is enclosed with two dashed lines. Nodes in the radial eigenfunction for such modes may occur in both the p- and g-mode propagation cavities.

The propagation diagram corresponding to the hotter template model ($T_{\rm eff} \sim 9500$ K) is displayed in Fig. 3. Although the chemical profiles have not changed as compared with the cooler template model, the Brunt-Väisälä frequency exhibits changes due to the higher effective temperature. Specifically, N^2 is larger at the outer regions, pushing the frequencies of the p modes and some mixed modes to higher values (shorter periods). In addition, this model has two thin convective regions in the outer parts of the star, in contrast to the single and very wide convection zone characterizing the cooler template model (see Fig. 2).

3.1.2. Excitation mechanism, driving and damping processes

The normalized growth rate η ($\equiv -\Im(\sigma)/\Re(\sigma)$, where $\Re(\sigma)$ and $\Im(\sigma)$ are the real and the imaginary part, respectively, of the complex eigenfrequency σ) in terms of pulsation periods Π for overstable $\ell = 1$ modes corresponding to the cool template model ($T_{\rm eff} \sim 7400$ K) is shown in the upper panel of Fig. 4. The lower panel shows the results for the hot template model ($T_{\rm eff} \sim 9500$ K). A value of $\eta > 0$ ($\eta < 0$) implies unstable

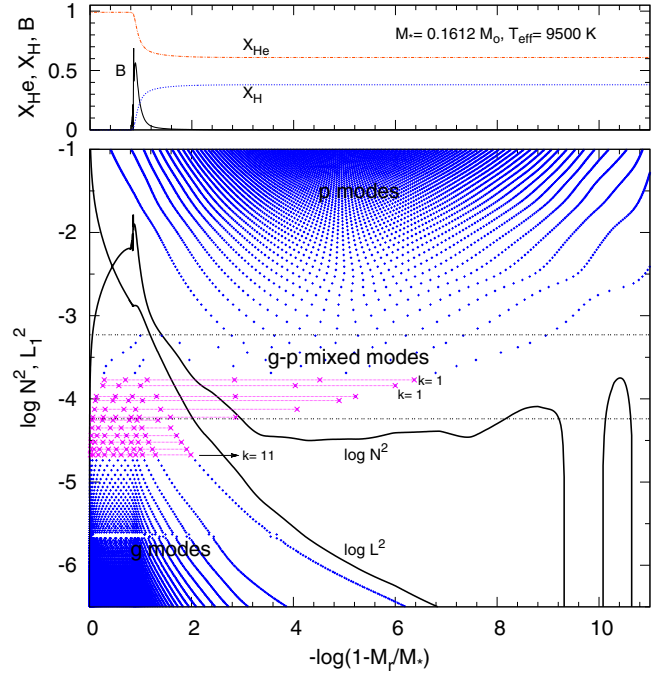(stable) modes. We emphasize with red dots the unstable modes. The nodes of unstable modes are highlighted in Figs. 2 and 3 with a "×" symbol (in magenta) and connected with thin lines. In Fig. 4, the vertical dashed lines enclose the period interval of mixed $p - g$ modes. As can be seen from the figure, the set of unstable modes for both template models include some "pure" g modes and some g mixed modes[5]. No pure p mode nor p mixed mode is excited in the cool template model, although a p mixed mode (that having $k = 1$) is driven in the hot template model. According to Fig. 4, within a given band of unstable modes, the excitation is markedly stronger (large values of η) for the lowest-order g mixed modes, characterized by short periods (high frequencies). We note that the band of excited modes in the cool template model ($800\ {\rm s} \lesssim \Pi \lesssim 3150\ {\rm s}$) is substantially wider than that of the hot template model ($400\ {\rm s} \lesssim \Pi \lesssim 1400\ {\rm s}$).

In order to investigate the details of the damping/driving processes and to identify the excitation mechanism responsible for the destabilization of modes in our pre-WD models, we selected two representative pulsation modes of each template model. The results described below are also typical of all other modes of interest. Specifically, we choose the unstable g mixed mode with $k = 5$ and the stable p mixed mode with $k = 5$ for both template models. These modes are marked with arrows in Fig. 4. In the left panels of Fig. 5 we depict the differential work function ${\rm d}W/{\rm d}r$ and the running work integral W (computed as in Lee & Bradley 1993) for the unstable $k = 5$ g mixed mode (stable $k = 5$ p mixed mode), characterized by $\Pi = 1091\ {\rm s}$, $\eta = 6.7 \times 10^{-6}$ ($\Pi = 604.7\ {\rm s}$, $\eta = -1.03 \times 10^{-5}$) in the upper (lower) panel, corresponding to our cool template model ($T_{\rm eff} \sim 7400$ K). The results for the hot template model ($T_{\rm eff} \sim 9500$ K) are displayed in the

---

[5] We classify as "g mixed modes" those mixed modes that have most of their nodes laying in the g-mode propagation cavity, and as "p mixed modes" those mixed modes having most of their nodes in the p-mode propagation cavity.
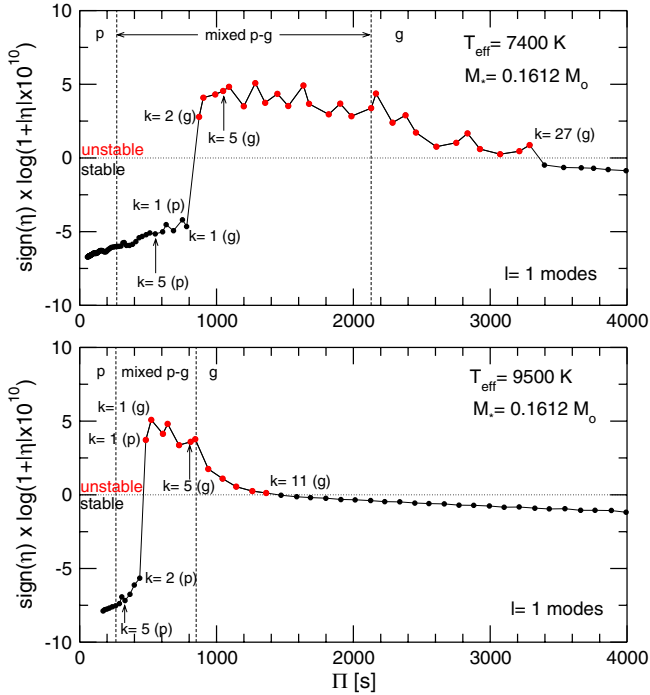
Fig. 4. Normalized growth rates η for $\ell = 1$ p and g modes in terms of the pulsation periods for the 0.1612 $M_\odot$ pre-WD template model at $T_{\rm eff} = 7400$ K (*upper panel*) and the 0.1612 $M_\odot$ pre-WD template model at $T_{\rm eff} = 9500$ K (*lower panel*). The large numerical range spanned by η is appropriately scaled for a better graphical representation. Some specific modes are labeled. The g and p modes with $k = 5$ are analyzed in Fig. 5. The vertical dashed lines enclose the period interval of mixed $p - g$ modes. Unstable modes are emphasized with red dots.

right panels, being in this case $\Pi = 810.4$ s and $\eta = 3.9 \times 10^{-7}$ for the unstable $k = 5$ g mixed mode, and $\Pi = 330.9$ s and $\eta = -1.5 \times 10^{-3}$ for the stable $k = 5$ p mixed mode. The scales for dW/dr and W are arbitrary. Also shown is the Rosseland opacity (κ) and its derivatives $[\kappa_T + \kappa_\rho/(\Gamma_3 - 1)]$, and the logarithm of the thermal timescale ($\tau_{\rm th}$). We restrict the figures to the envelope region of the models, where the main driving and damping processes occurs.

We first concentrate on the hot template model (right panels of Fig. 5). The region that destabilizes the modes (where $dW/dr > 0$) is clearly associated with the bump in the opacity due to the He$^+$ partial ionization zone ($\log T \sim 4.7$) that involves the second ionization of He (He$^+ \leftrightarrow$ He$^{++} + e^-$). We note the presence of a convection zone at that region (gray area in the figure), centered at $-\log q \sim 9.7$ [$q \equiv (1 - M_r/M_\star)$]. The thermal timescale reaches values in the range $\sim 150-1500$ s at the driving region, in agreement with the period interval of unstable modes for this template model (400–1400 s). In the driving region the quantity $\kappa_T + \kappa_\rho/(\Gamma_3 - 1)$ is increasing outwards, in agreement with the well known necessary condition for mode excitation (Unno et al. 1989). For the unstable g mixed mode, the contributions to driving at $-\log q$ from ~ 9.1 to ~ 10.6 (where $dW/dr > 0$) largely overcome the damping effects at $-\log q \lesssim 9$ (where $dW/dr < 0$), as reflected by the fact that $W > 0$ at the surface, and therefore the mode is globally excited. In contrast, the strong damping experienced by the p mode (denoted by negative values of dW/dr at $8 \lesssim -\log q \lesssim 9.3$ and $-\log q \gtrsim 9.8$) makes this mode globally stable. We note that there exists a second, external convective zone, that corresponds to the partial ionization region where both the ionization of neutral H (H $\leftrightarrow$ H$^+ + e^-$) and the first

ionization of He (He $\leftrightarrow$ He$^+ + e^-$) occurs ($\log T \sim 4.15-4.42$). Since it is located very close to the stellar surface, the presence of these partial ionization zones is completely irrelevant in destabilizing modes.

We turn now to the case of the cool template model (left panels of Fig. 5). At variance with the hot template model, in this case there is a single and wide outer convection zone, that extends from $-\log q \sim 6.6$ outwards. The opacity is characterized by three bumps, one is located at $-\log q \sim 7.9$ and associated with the second ionization of He, another at $-\log q \sim 9$ corresponding to the first ionization of He, and the third is at $-\log q \sim 9.5$ and associated with the ionization of neutral H. We note that, since the regions of the ionization of H and the first ionization of He are located deeper in the star as compared with the case of the hot template model, they now play a role in the destabilization of modes. Indeed, the three bumps in κ are responsible for the strong driving of the unstable g mixed mode, as indicated by the positive values of the differential work function at those regions, that largely exceeds the damping at $-\log q \sim 8.4$ and to a less extent at $-\log q \sim 9.4$ and ~ 9.9. For the stable p mixed mode, the driving and damping regions are located at almost the same places in the star as for the unstable g mixed mode, i.e., the function dW/dr exhibits roughly the same shape. What makes the difference, however, is the very strong damping experienced by this mode at the surface regions ($-\log q \gtrsim 9.7$), where dW/dr adopts large and negative values, which render the mode globally stable.

In summary, we identify the $\kappa - \gamma$ mechanism associated with the opacity bump due to partial ionization of He$^+ -$ He^{++} centered at $T \sim 5 \times 10^4$ K as a destabilizing agent for the unstable pulsation modes of our hot pre-WD models, which are represented by the template model at $T_{\rm eff} \sim 9500$ K (right upper panel of Fig. 5). This is in agreement with the predictions of the radial-mode instability results of Jeffery & Saio (2013; see Sect. 3.1.4). We note that the extension (in $T_{\rm eff}$) of the instability domain is sensitive to the abundance of He at the driving region, which in turn, depends on the stellar mass and possibly to the detailed previous binary evolution. In Fig. 6 we show the He abundance (upper panel) and the Rosseland opacity (lower panel) in terms of the logarithm of the temperature, corresponding to models at $T_{\rm eff} \sim 9000$ K and different stellar masses. We emphasize with a vertical gray strip the driving region of the models ($\log T \sim 4.7$). The abundance of He at the driving region monotonically decreases with increasing stellar mass (upper panel). Also, the density at the driving region diminishes for higher masses. Thus, because He is less abundant and density is lower for stellar models characterized by higher masses, the bump in the opacity at the region of the He$^+ -$ He^{++} partial ionization zone decreases in magnitude for increasing stellar mass. This translates in a weaker capability to destabilize modes. Ultimately, for models with masses $M_\star/M_\odot \geq 0.2390$ and $T_{\rm eff} \sim 9000$ K the He abundance is so low (and the bump in the opacity has decreased to such an extent) that there is no pulsational instability, and models in that range of masses do not exhibit excited modes (see Fig. 1).

On the other hand, we have found that for the cool pre-WD models, represented by our template model at $T_{\rm eff} \sim 7400$ K (left upper panel of Fig. 5), the $\kappa - \gamma$ mechanism is efficient to destabilize modes. This time, however, the $\kappa - \gamma$ mechanism not only works due to the partial ionization of He$^+ -$ He^{++} ($T \sim 5 \times 10^4$ K), but instead also due to the presence of the bumps in κ associated with the partial ionization of He$-$ He$^+$ and H$-$ H$^+$, located at $T \sim 2.6 \times 10^4$ and $T \sim 1.4 \times 10^4$ K, respectively.
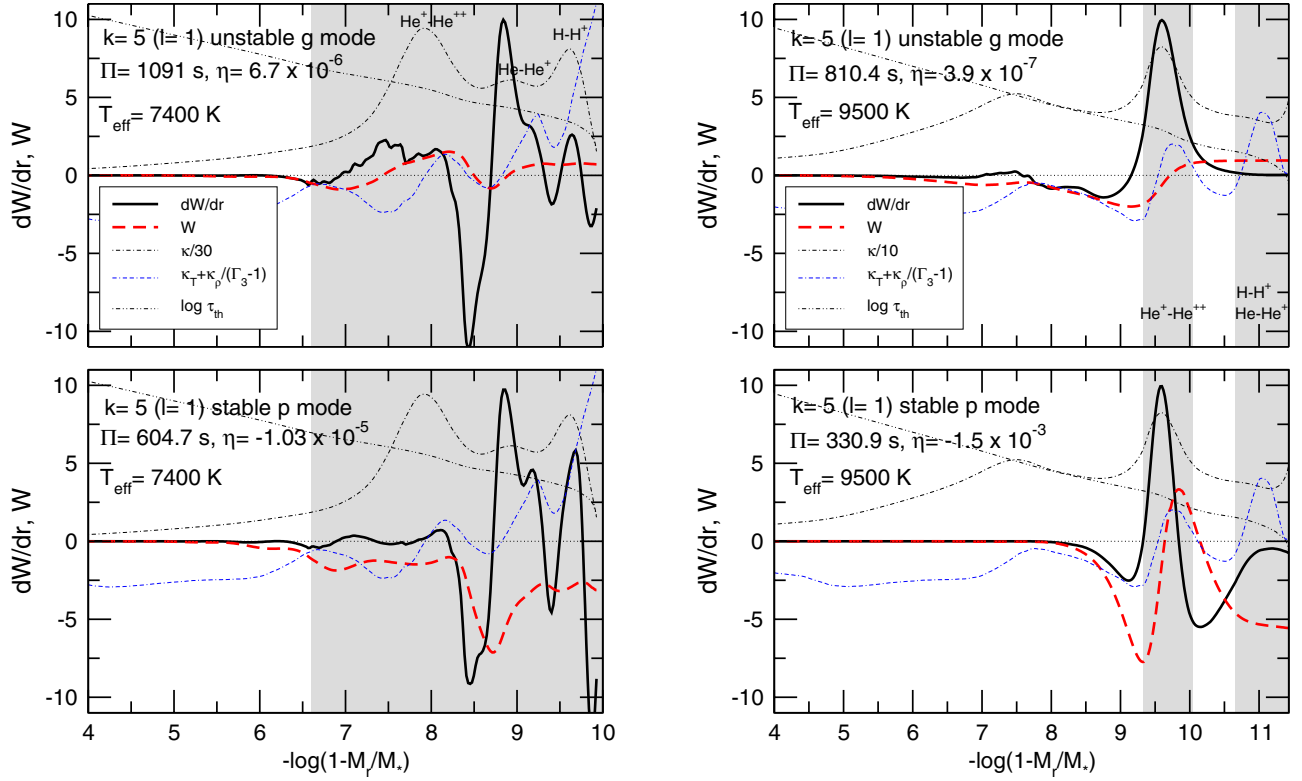
Fig. 5. *Left panels*: the differential work (dW/dr) and the running work integral (W) for the unstable g mode with $k = 5$ (*upper panel*) and the stable p mode with $k = 5$ (*lower panel*), along with the Rosseland opacity profile (κ), the opacity derivatives, and the thermal timescale ($\tau_{\rm th}$) of our $0.1612\,M_\odot$ pre-WD template model at $T_{\rm eff} = 7400$ K. The gray areas show the location of the convection zones due to the partial ionization zones. *Right panels*: same as in the left panels, but for the $0.1612\,M_\odot$ pre-WD template model at $T_{\rm eff} = 9500$ K.
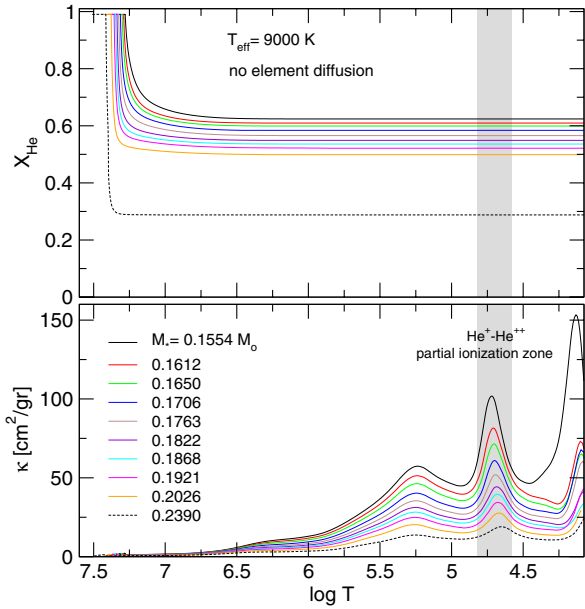
Fig. 6. He abundance (*upper panel*) and the Rosseland opacity (*lower panel*) in terms of the logarithm of the temperature, corresponding to models at $T_{\rm eff} \sim 9000$ K and different stellar masses indicated in the plot. The vertical gray strip is the location of the region of mode driving ($\log T \sim 4.7$).

3.1.3. Instability domains

A more comprehensive view of the pulsational stability properties of our models can be accomplished by examining the range
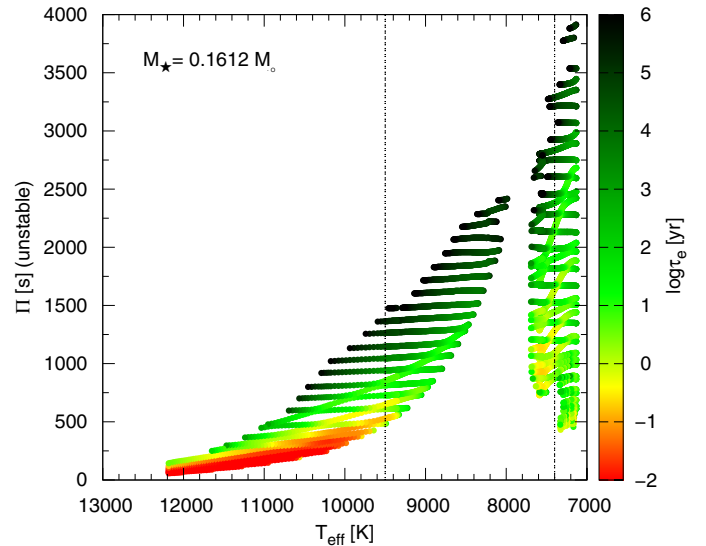

Fig. 7. Unstable $\ell = 1$ mode periods (Π) in terms of the effective temperature, corresponding to the pre-WD model sequence with $M_\star = 0.1612\,M_\odot$. Color coding indicates the value of the logarithm of the e-folding time (τ_e) of each unstable mode (right scale). The vertical lines indicate the effective temperatures of the template models analyzed in Figs. 2–5.

of unstable periods of our template model for the full range of effective temperatures. In Fig. 7 we show the instability domains of $\ell = 1$ periods in terms of the effective temperature for the pre-WD model sequence with $M_\star = 0.1612\,M_\odot$. The palette of colors (right scale) indicates the value of the logarithm of the

e-folding time (in years) of each unstable mode. The vertical lines correspond to the effective temperatures of the two template models described in Figs. 2−5. The e-folding time, defined as $\tau_e = 1/|\mathfrak{I}(\sigma)|$, is an estimate of the time it would take a given mode to reach amplitudes large enough as to be observable. It has to be compared with the evolutionary timescale which represents the time that the model spends evolving in the regime of interest. In the case displayed in Fig. 7, $\tau_{instability} \sim 1.3 \times 10^9$ yr, $\tau_{instability}$ being the time it takes the 0.1612 $M_\odot$ model to evolve from $T_{eff} \sim 7200$ K to $T_{eff} \sim 12\,400$ K (Table 1). We note that $\tau_{instability} \gg \tau_e^{max} \sim 10^6$ yr. Thus, our calculations show that there is plenty of time for the destabilization of any of the pulsation modes shown in the Figure, and to achieve observable amplitudes while the star is in the instability domain.

Two different and separated domains of instability can be clearly distinguished in the Fig. 7. One of them, at high temperatures, corresponds to modes destabilized by the $\kappa-\gamma$ mechanism associated with the second ionization of He. The other domain, at lower effective temperatures, is associated with the $\kappa-\gamma$ mechanism in which, in addition to the second ionization of He, there are appreciable contributions from the first ionization of He and the ionization of H, as we have discussed before. Notably, there are evident signatures of avoided crossings in both instability domains.

For the high-T_{eff} domain, among the unstable modes, the strongest excitation (that is, the smallest e-folding time, emphasized with light red and yellow zones in the plot) corresponds to short periods in the range 150 s−600 s associated with low-order $p-g$ mixed modes. Intermediate- and high-order g modes with periods $\Pi \gtrsim 600$ s are also driven, but with much longer e-folding times (light and dark green). The trend of shorter excited periods for higher effective temperatures that characterizes the instability domain in the $T_{eff} - \Pi$ plane (see Fig. 7) can be explained in terms of the precise location of the driving region in the interior of the model and the thermal timescale at that region. Specifically, as the star contracts and evolves towards higher effective temperature, the partial ionization zone of He^+-He^{++} shifts toward layers located closer to the stellar surface, where the thermal timescale is shorter. Thus, as the T_{eff} of the star increases, the $\kappa-\gamma$ mechanism is able to excite modes with gradually shorter periods. Eventually, when the partial ionization zone of He^+-He^{++} is very close to the stellar surface, it loses the ability to destabilize modes, giving place to the hot edge of the instability domain.

We focus now on the instability domain at lower T_{eff}. This instability region is characterized by much wider ranges of excited modes, as compared to the main instability region at higher T_{eff}. We note that there exists a gap in effective temperature, separating both instability domains, in which no unstable modes exist. As described above, at low effective temperatures ($T_{eff} \lesssim 7800$ K), the partial ionization regions of $H-H^+$ and $He-He^+$ are far enough from the stellar surface such that they contribute substantial driving, adding to that from the He^+-He^{++} partial ionization zone. As a result of this, the driving region is fairly wide, which translates to a very broad range of unstable periods. As the star evolves and heats up, the opacity bump corresponding to the He^+-He^{++} partial ionization zone drops significantly, while the partial ionization region of $H-H^+$ and $He-He^+$ shifts towards the stellar surface. Both effects result in a strong weakening of the total driving, leading to an instability domain that is quite restricted in the $T_{eff} - \Pi$ plane or that can even disappear altogether. As the star heats up more, the partial ionization region of He^+-He^{++} eventually becomes efficient enough again as to destabilize modes, giving origin to the main instability region, at high T_{eff}, as described before.

The dependence described above between the periods of unstable $\ell = 1$ modes and the T_{eff} of the models holds for all of our pre-WD sequences, as is apparent from Fig. 8. In this multiple-panel array we show the unstable modes on the $T_{eff} - \Pi$ plane for the evolutionary sequences with masses $M_\star/M_\odot = 0.1554, 0.1612, 0.1650, 0.1706, 0.1763, 0.1822, 0.1868, 0.1921,$ and 0.2026. The sequence with $M_\star = 0.2390\,M_\odot$ (not included in the figure) exhibits unstable models with periods longer than $\sim$13 000 s. More massive model sequences do not show unstable modes for the range of effective temperatures explored ($T_{eff} \gtrsim 6000$ K). It is important to mention that, at effective temperatures higher than $\sim$6000 K, there exist pulsating stars with modes that appear to be excited either stochastically or coherently by near surface convection, an example being the δ Scuti star HD 187547 ($T_{eff} \sim 7500$ K, $\log g \sim 3.90$; Antoci et al. 2011, 2014). So, it is not inconceivable that some pulsation modes detected in low-mass pre-WD stars can be driven not by the $\kappa-\gamma$ mechanism, but by stochastic excitation instead.

In Fig. 8 we have employed a logarithmic scale for the periods in order to enhance the short-period regime of the $T_{eff} - \Pi$ diagrams. The figure shows the presence of the two instability regions described before for $M_\star/M_\odot \leq 0.1868$. We note that both regions are separated for $M_\star/M_\odot \leq 0.1763$, but they merge into one for sequences with larger masses. In general, both p and g modes are excited in our pre-WD models, including modes with mixed character (p and g; see Figs. 2−4). The longest excited periods reach values in excess of $\sim$15 000 s for the highest-mass sequence showing unstable modes ($M_\star/M_\odot = 0.2026$), and this limit drastically decreases to $\sim$3000 s for the less massive sequence ($M_\star/M_\odot = 0.1554$) considered. The shortest excited periods, in turn, range from $\sim$50 s for $M_\star/M_\odot = 0.1554$, to $\sim$3000 s for $M_\star/M_\odot = 0.2026$. So, the longest and shortest excited periods are larger for higher $M_\star$. We note that for the case of $\ell = 2$ modes, the longest and shortest periods are somewhat shorter than for $\ell = 1$ modes. We note that, in the case of the sequences with $M_\star/M_\odot = 0.1554, 0.1650$ and 0.1612, the stellar models still display excited modes even after reaching their maximum effective temperature (see Fig. 1) and entering their cooling tracks. For clarity, we have not included in Fig. 8 the unstable periods associated with these stages. Regarding the strength of the mode instability, we found that, for each mass considered, the modes with shorter periods are the most strongly excited, with e-folding times as short as $\tau_e \sim 0.01-1$ yr). In contrast, modes with longer periods are much more weakly destabilized, and e-folding times can be as large as $\tau_e \sim 10-10^6$ yr, although still much shorter than the time it takes models to cross the instability domains, i.e., $\tau_e \ll \tau_{instability}$ (see Table 1).

Figure 9 is the counterpart of Fig. 8 but for radial ($\ell = 0$) modes. It may be noted that, although the trends are the same as for nonradial modes with $\ell = 1$, in the case of radial modes there are many fewer modes excited. This trend is more pronounced for higher masses. In the case of the high-T_{eff} instability domain, radial modes with $k = 0, 1, 2, 3, 4$ are excited for the sequence with $M_\star = 0.1554\,M_\odot$, whereas for sequences more massive than $0.1822\,M_\odot$, only the fundamental radial ($k = 0$) mode is excited. On the other hand, in the case of the low-T_{eff} instability domain, a modestly higher number of radial modes are excited. Finally, we note that the blue edge of the radial-mode instability domain is substantially cooler than that of nonradial $\ell = 1$ modes (see Fig. 1).
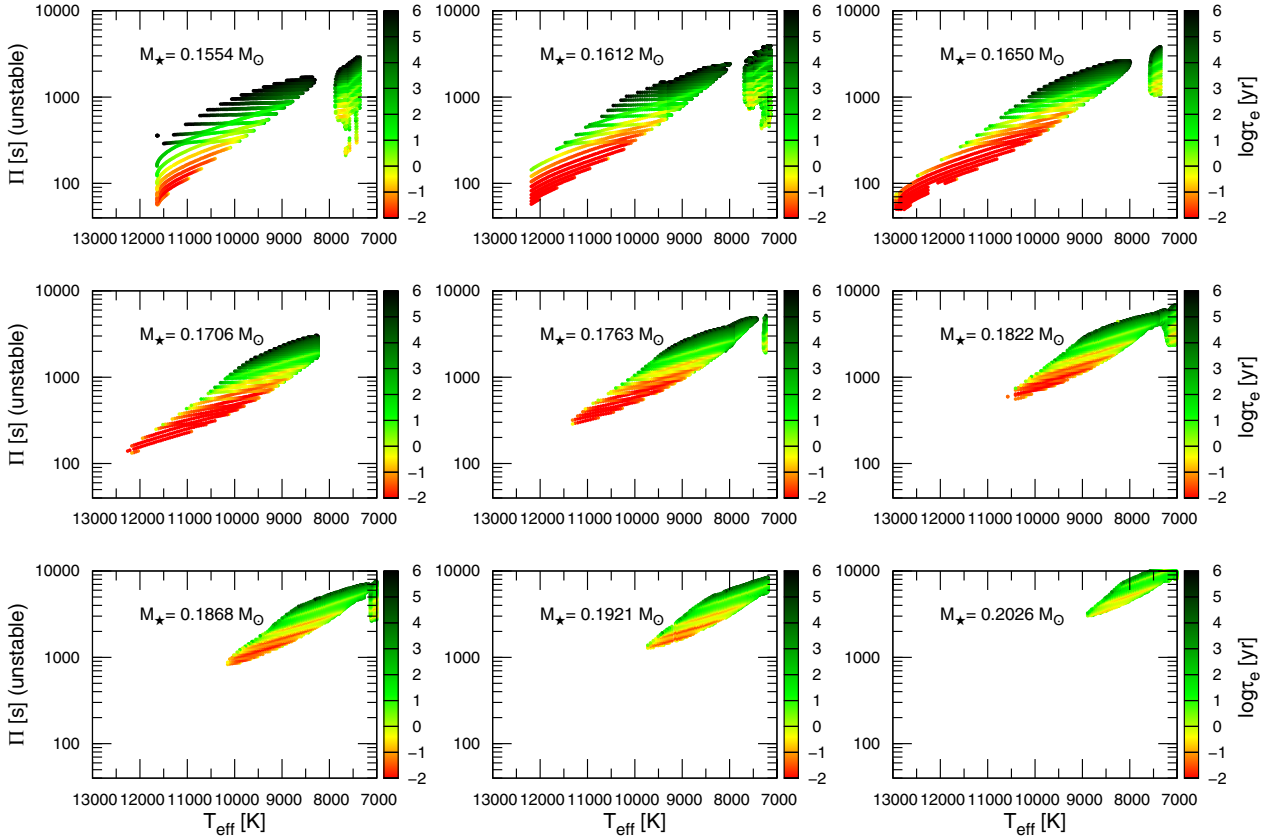
Fig. 8. Unstable mode periods (Π) for $\ell = 1$ in terms of the effective temperature, corresponding to the pre-WD model sequences with stellar masses $M_\star/M_\odot = 0.1554, 0.1612, 0.1650, 0.1706, 0.1763, 0.1822, 0.1868, 0.1921$, and 0.2026. Color coding indicates the value of the logarithm of the e-folding time (τ_e) of each unstable mode (right scale).

3.1.4. Comparison with the Jeffery & Saio (2013)'s results

Jeffery & Saio (2013) have performed a detailed exploration of radial-mode ($\ell = 0$) pulsation stability of low-mass pre-WD stars across a range of composition, effective temperature and luminosity. They present their results in terms of the instability domains in the $\log T_{\mathrm{eff}} - \log[(L_\star/L_\odot)/(M_\star/M_\odot)]$ space. In order to make a comparison with our own results, we transform their results to the $T_{\mathrm{eff}} - \log g$ plane. Jeffery & Saio (2013) employ a set of static envelope models with uniform compositions of $X_H = 0.90, 0.75, 0.50, 0.25, 0.01$ and 0.002 and a basic metal mass fraction $Z = 0.02$. This implies He fractional abundances of $X_{\mathrm{He}} = 0.08, 0.23, 0.48, 0.73, 0.97$ and 0.978. Since our evolutionary models are characterized by $0.49 \lesssim X_{\mathrm{He}} \lesssim 0.62$ in the mass range $0.1554 \lesssim M_\star/M_\odot \lesssim 0.2026$ (see Fig. 6), we can compare our results with those of Jeffery & Saio (2013) for the case $X_H = 0.50$ ($X_{\mathrm{He}} = 0.48$).

In Fig. 10 we show the same $T_{\mathrm{eff}} - \log g$ diagram presented in Fig. 1 but this time including a gray area that represents the results of Jeffery & Saio (2013) for their radial-mode instability domain for static envelope models with a H fractional mass of $X_H = 0.50$ ($X_{\mathrm{He}} = 0.48$), as depicted in the upper right panel of their Figure 1. The region enclosed by the instability boundaries includes models with at least one unstable radial mode. We note that the instability domain predicted by our calculations (both for radial and nonradial modes) is contained within the instability domain of Jeffery & Saio (2013). We note, however, that our radial-mode blue edge is cooler (∼800 K) than the blue edge of the Jeffery & Saio (2013) instability domain. Notably, it is our nonradial-mode blue edge ($\ell = 1, 2$) which is in excellent

agreement with the radial-mode blue edge of those authors. The discrepancy between our $\ell = 0$ blue edge and that of Jeffery & Saio (2013) could be explained, in part, on the basis that our models have a He abundance at the driving region which is dependent on the stellar mass, while the models of Jeffery & Saio (2013) have a fixed He abundance ($X_{\mathrm{He}} = 0.48$). On the other hand, there is a notable agreement between the two sets of calculations in relation to the unstable region where the partial ionization of H–H$^+$ and He–He$^+$ contributes to the destabilization of modes. Indeed, in Fig. 10 the hot boundary of the instability "finger" at $7800 \lesssim T_{\mathrm{eff}} \lesssim 9000$ K and $4.5 \lesssim \log g \lesssim 6$ of Jeffery & Saio (2013) nearly matches the extension of the dot-dashed lines corresponding to our computations.

In summary, given that both sets of computations were performed independently using different evolutionary and pulsation codes, and very distinct stellar models, and in spite of the discrepancy in the location of the radial-mode blue edges, the agreement between the results of Jeffery & Saio (2013) and ours is encouraging.

3.2. Computations with element diffusion

We have redone all of our evolutionary and stability pulsation computations by taking into account the action of element diffusion, as in Althaus et al. (2013). In Fig. 11 we present a $T_{\mathrm{eff}} - \log g$ plane showing the resulting low-mass He-core pre-WD evolutionary tracks (dotted curves) computed considering element diffusion. The evolutionary tracks with element diffusion are substantially different to the case in which this process
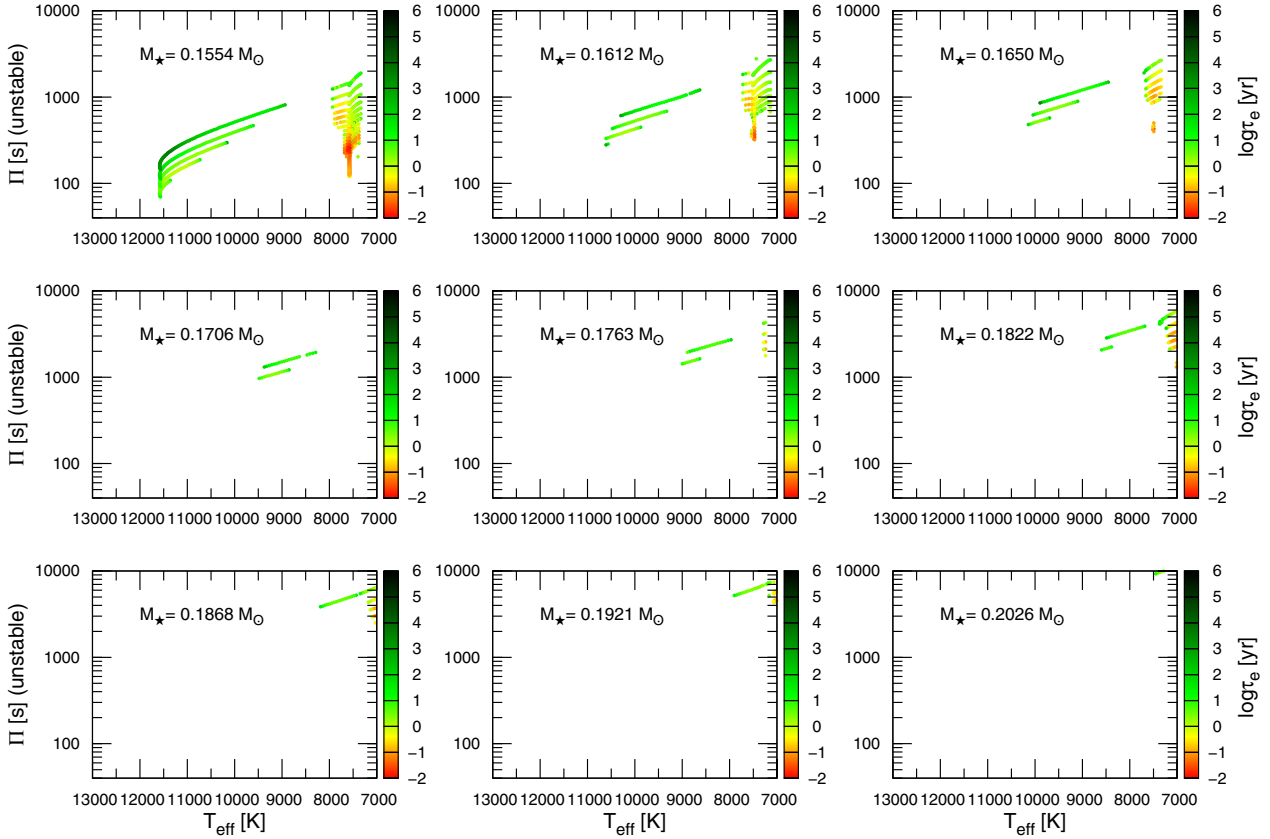
Fig. 9. Same as Fig. 8, but for radial ($\ell = 0$) modes.

is neglected. In particular, diffusion tracks are displaced to lower $T_{\rm eff}$ and $\log g$ as compared with nondiffusion tracks, as it can be realized by comparing Fig. 11 with Fig. 1 (see also Fig. 10). This is because, for a given surface luminosity value, models with element diffusion have lower effective temperature and thus larger radii because H diffuses upwards during the course of evolution (see Althaus & Benvenuto 2000; Althaus et al. 2001).

Figure 11 demonstrates emphatically that when element diffusion is taken into account in low-mass He-core pre-WD models, the pulsational instability region is much more restricted than in the case of nondiffusion models. This can be understood as follows. When the models, which are evolving towards higher effective temperatures, are still cool enough, there is strong driving due to the $\kappa - \gamma$ mechanism acting at the three partial ionization regions present in the stellar envelope: $\rm He^+ - He^{++}$ ($\log T \sim 4.7$), $\rm He - He^+$ ($\log T \sim 4.42$), and $\rm H - H^+$ ($\log T \sim 4.15$). However, as element diffusion operates, H begins to migrate to the surface and He starts to sink toward deeper layers. The increasing deficit of He strongly weakens the driving due to the $\rm He^+ - He^{++}$ and $\rm He - He^+$ partial ionization zones, while the driving due to the $\rm H - H^+$ partial ionization zone becomes progressively important. When $X_{\rm He}$ drops below a certain critical value at the driving regions, pulsational instabilities are due exclusively to the $\rm H - H^+$ partial ionization zone. While this zone is located far enough from the surface, the driving will continue due to the $\kappa - \gamma$ mechanism. However, this partial ionization region migrates towards the stellar surface as the star – while evolving to higher $T_{\rm eff}$ – heats up. Consequently, the efficiency of driving is weakened, until the instability ceases. The blue edge appears at that stage. All this process involves a rather discrete range in $T_{\rm eff}$ (~1000 K), and this is the reason for which the
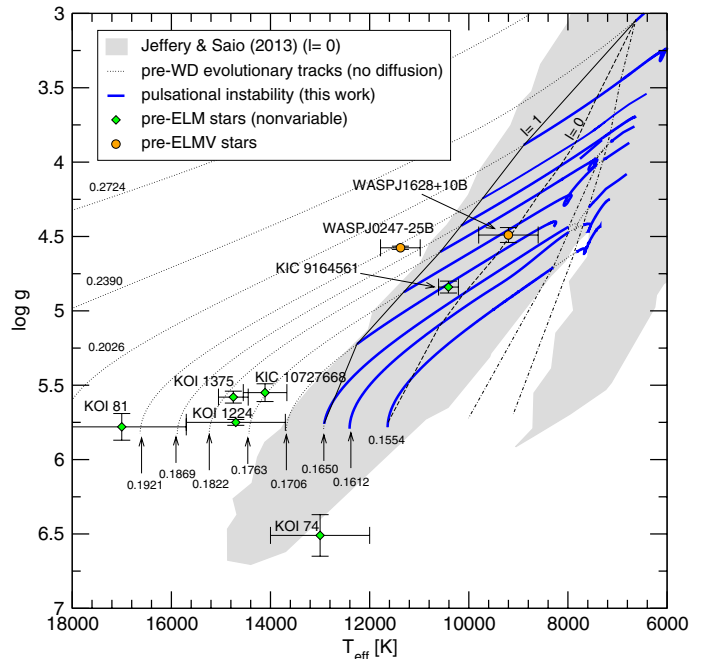

Fig. 10. Same as Fig. 1, but including the radial mode ($\ell = 0$) instability domain (gray area) computed by Jeffery & Saio (2013) for the case of static envelope models with a H fractional mass of $X_{\rm H} = 0.50$ ($X_{\rm He} = 0.48$) (*upper right panel* of their Fig. 1).

instability domain is so narrow. This is clearly shown in Fig. 11 by means of thick blue lines that mark the portions of the evolutionary tracks corresponding to stellar models having unstable
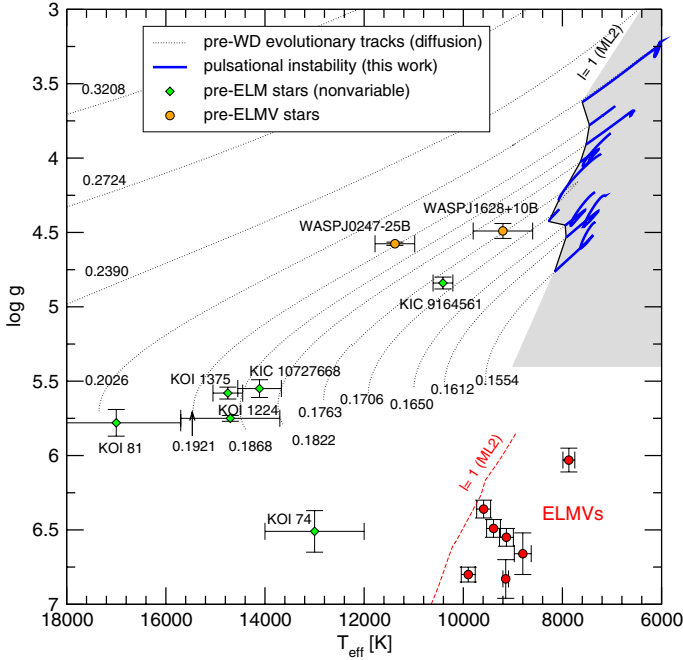
Fig. 11. Same as Fig. 1, but for the case in which the low-mass He-core pre-WD models are computed by taking into account element diffusion. The evolutionary tracks are marked with dotted curves.

Fig. 12. He abundance (*upper panel*) and the Rosseland opacity (*lower panel*) in terms of the outer mass fraction coordinate, corresponding to models with $M_\star = 0.1868 \, M_\odot$ with element diffusion and different (increasing) values of T_{eff}, which are marked in Fig. 13. Solid curves correspond to models in which there is pulsation instability, while dashed curves are associated with models in which instability has ceased. The tops of the bumps in the opacity due to the He^+-He^{++}, $He-He^+$, and $H-H^+$ partial ionization regions are connected with thin dotted lines, to show their evolution.

modes. For illustrative purposes, we extrapolate the instability region (gray area) to lower and higher gravities, and to lower effective temperatures.

In the upper panel of Fig. 12 we show the He abundance in terms of the outer mass fraction for different effective temperatures during the evolution of 0.1868 $M_\odot$ pre-WD models when element diffusion is taken into account. The lower panel shows the Rosseland opacity for the same evolutionary stages. As might be expected, the contribution of the He^+-He^{++} and $He-He^+$ κ bumps strongly diminishes as the abundance of He drops at the locations of the corresponding partial ionization zones, to the point that for $T_{\text{eff}} \sim 7060$ K these bumps have vanished. At the same time, the κ bump due to the $H-H^+$ partial ionization zone maintains its value almost constant, and remains the only source of mode excitation. For higher effective temperatures, this bump moves towards the stellar surface, gradually losing its ability to excite modes through the $\kappa - \gamma$ mechanism. For $T_{\text{eff}} \gtrsim 7400$ K, pulsational excitation by this partial ionization region ceases (dashed curves) and all the modes become pulsationally stable. All this process also can be appreciated in the $\Pi - T_{\text{eff}}$ plane, as depicted in Fig. 13, in which we show the evolution of the $\ell = 1$ unstable mode periods corresponding to the model sequence with $M_\star = 0.1868 \, M_\odot$. Vertical dashed lines indicate the T_{eff} values considered in Fig. 12. For $T_{\text{eff}} \gtrsim 7000$ K, the unstable modes shown in the figure are destabilized by the $H-H^+$ partial ionization zone solely. Interestingly enough, modes with periods in the range $2000 \lesssim \Pi \lesssim 5000$ s are strongly destabilized, as can be appreciated from the light red and yellow zones associated with very short e-folding times.

4. Comparison with the observed pre-ELMVs

At present, only two variable stars identified as pulsating pre-ELM WD objects have been detected. They are plotted in Figs. 1, 10, and 11. We include in these figures six nonvariable pre-ELM WDs observed in the *Kepler* mission field. The
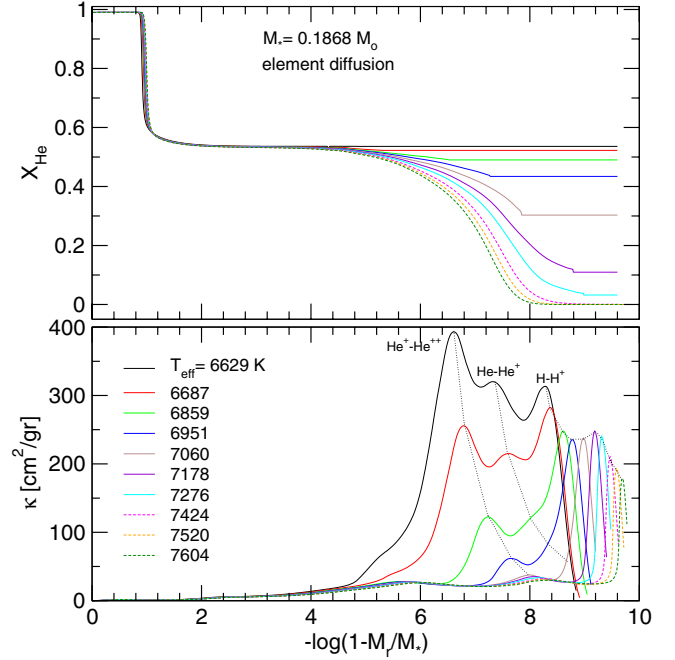
pulsating stars are WASP J0247−25B, with spectroscopic parameters of $T_{\text{eff}} = 11\,380 \pm 400$ K and $\log g = 4.576 \pm 0.011$ (Maxted et al. 2013), and WASP J1628+10B, characterized by $T_{\text{eff}} = 9\,200 \pm 600$ K, $\log g = 4.49 \pm 0.05$ (Maxted et al. 2014)[6].

From Sect. 3.2, we note that our theoretical computations with element diffusion do not account for any of the observed pulsating pre-ELM WD stars. We conclude that, on the basis of our nonadiabatic pulsation models, element diffusion does not operate in low-mass pre-WD stars, at least in the frame of the binary evolution model assumed in our study for the evolutionary history of progenitor stars. Several factors could play a role in preventing (or undermining) the effects of element diffusion, including stellar winds (Unglaub & Bues 2000) and/or stellar rotation (Strittmatter & Wickramasinghe 1971). As interesting as these topics are in this context, their exploration is beyond the scope of this investigation and they will be addressed in future studies.

The remainder of the discussion in this section is focused on the comparison between the observed properties of the target stars and the predictions emerging from our stability analysis based on nondiffusion models that have been explored at length in Sect. 3.1. Figure 1 shows that for these models, WASP J1628+10B is located within the theoretical instability domains. As for WASP J0247−25B, it is hotter than the blue edges ($\ell = 0, 1, 2$) of the instability domain in the $T_{\text{eff}} - \log g$ plane (Fig. 1). On the other hand, of the six nonvariable pre-ELM

---

[6] The primary stars in both cases are A-type stars (showing δ Scuti pulsations), while in our computations we consider that the primary star of the initial binary system is a neutron star. We emphasize that we treat the neutron star essentially as a tool for stripping the envelope from the pre-WD star (Althaus et al. 2013).
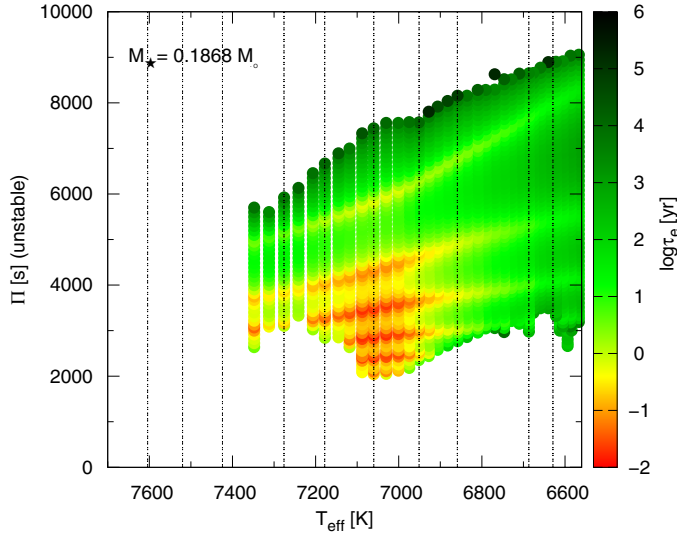
Fig. 13. Unstable $\ell = 1$ mode periods (Π) in terms of the effective temperature, corresponding to the pre-WD model sequence with $M_\star = 0.1868\,M_\odot$. Color coding indicates the value of the logarithm of the e-folding time (τ_e) of each unstable mode (right scale). The vertical dashed lines indicate the effective temperatures of the models analyzed in Fig. 12.

Fig. 14. Periods of unstable $\ell = 1$ modes in terms of the effective temperature, with the palette of colors (right scale) indicating the value of the logarithm of the e-folding time (in years), corresponding to the sequences with $M_\star = 0.1706\,M_\odot$ (small dots) and $M_\star = 0.1763\,M_\odot$ (large dots) neglecting element diffusion. Also shown are the pulsation periods of the pre-ELM WD star WASP J1628+10B (horizontal segments).

WDs considered, five of them fall outside the theoretical instability strip, and only one (KIC 9164561) is oddly located within the nonradial instability region.

Below, we first explore the excited period spectrum of WASP J1628+10B in the context of our nondiffusion stability computations. Then we consider the possibility of whether a higher He abundance at the driving regions in our models would extend the blue edge of the instability domain in order to include WASP J0247−25B. Finally, we estimate how small the abundance of He at the driving region of KIC 9164561 must be in order to inhibit the pulsations in this star.

4.1. WASP J1628+10B

According to Maxted et al. (2014), this star exhibits pulsations with periods at 668.6 s and 755.2 s. The effective temperature and gravity situate WASP J1628+10B within the theoretical instability domain derived in this work (Fig. 1). According to its location in the $T_{\rm eff} - \log g$ diagram, we can compare the periods observed in this star with the ranges of excited periods for the sequences with $M_\star = 0.1706\,M_\odot$ and $M_\star = 0.1763\,M_\odot$. In Fig. 14 we show the periods of unstable $\ell = 1$ modes for these two sequences in terms of the effective temperature, along with the pulsation periods of the pre-ELM WD star WASP J1628+10B. Notably, our theoretical computations are in good agreement with the observations. In particular, we obtain unstable modes with periods that closely match the periods measured in WASP J1628+10B at the right effective temperature range. We note that, according to our theoretical computations, the modes associated with the periods of WASP J1628+10B are among the most unstable modes, with very short e-folding times ($\tau_e \sim 0.01-1$ yr).

We have not considered radial modes in our comparison, since our computations for these stellar masses predict only the fundamental ($k = 0$) and first overtone ($k = 1$) radial modes to be unstable (see Fig. 9), with periods long in excess
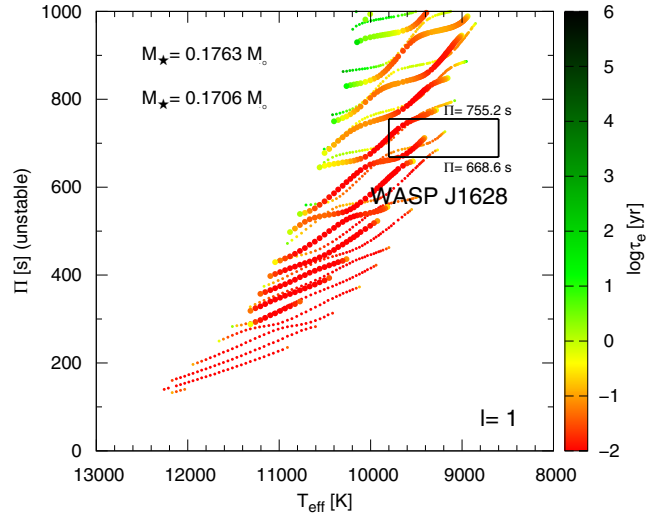
($\sim 1000-3000$ s) and therefore inconsistent with the periods observed in this star.

4.2. WASP J0247−25B

As mentioned, the pulsating pre-ELM WD star WASP J0247−25B (with periods at 380.95 s, 405.82 s, and 420.64 s) falls outside the pulsation instability domain computed in this work for nondiffusion models. This may be indicating that the He abundance in the driving region of the star is larger than our evolutionary computations predict. Also, part of this discrepancy could be attributed to the FC treatment employed in this work, that might be introducing uncertainties in the precise location of our blue edges. Here, we explore how large the He abundance should be to get pulsational instability at the right effective temperature and in the range of periods displayed by this star. With this aim, we evolve our pre-WD models up to the $T_{\rm eff}$ of the star, and then we artificially modify $X_{\rm He}$ at the location of the opacity bump due to the $\rm He^+ - He^{++}$ partial ionization zone. We perform nonadiabatic computations for increasing values of $X_{\rm He}$, starting with the canonical value predicted by the previous evolution. We restrict our analysis to nonradial $\ell = 1$ pulsation modes.

For WASP J0247−25B we have $T_{\rm eff} \sim 11\,380$ K and $\log g = 4.58$ (Maxted et al. 2013). As we can see from Fig. 1, the evolutionary tracks passing close to the star are those with masses $M_\star = 0.1868\,M_\odot$ and $M_\star = 0.1921\,M_\odot$. In Fig. 15 we display the normalized growth rates η for $\ell = 1$ modes as a function of the pulsation periods for $0.1868\,M_\odot$ pre-WD models at $T_{\rm eff} \sim 11\,400$ K (upper panel) and for $0.1921\,M_\odot$ pre-WD models at the same $T_{\rm eff}$ (lower panel). The vertical dashed lines correspond to the periods observed in WASP J0247−25B. In the figure, we use different symbols (connected with thin lines) to show the resulting η values for models with increasing He abundance at the driving region. The "canonical" He abundance (that predicted by the evolutionary computations) is $X_{\rm He} = 0.536$, being the corresponding H abundance of $X_{\rm H} = 0.453$. As can be seen, in this case (orange triangles up) all the pulsation modes are stable ($\eta < 0$). The same is true when we increase $X_{\rm He}$ to 0.60.
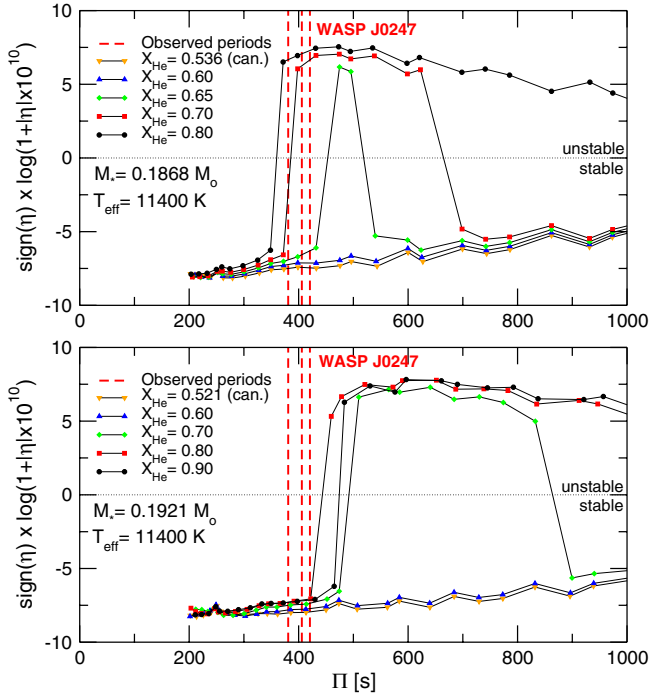
Fig. 15. Normalized growth rates η for $\ell = 1$ modes in terms of the pulsation periods for 0.1868 $M_\odot$ pre-WD models at $T_{\rm eff} \sim 11\,400$ K (*upper panel*) and for 0.1921 $M_\odot$ pre-WD models at the same $T_{\rm eff}$ (*lower panel*). Different symbols connected with thin lines are associated with models with different He abundance in the driving region, including that with canonical He abundance and those models (artificially modified) with increasing $X_{\rm He}$ values in that region (see text). The large numerical range spanned by η is appropriately scaled for a better graphical representation. The vertical dashed lines correspond to the periods at ∼381 s, ∼406 s, and ∼421 s observed in WASP J0247−25B.

For $X_{\rm H} = 0.65$ we obtain some unstable modes ($\eta > 0$), and the number of unstable modes increases as we increase $X_{\rm He}$. Similar results are depicted in the lower panel, corresponding to models with $M_\star = 0.1921\ M_\odot$. From the figure it is apparent that, in the case of the 0.1868 $M_\odot$ models (upper panel), in order to replicate the periods exhibited by WASP J0247−25B, the He abundance at the driving zone must be $X_{\rm He} \gtrsim 0.70$ ($X_{\rm H} \lesssim 0.29$). We note that the range of excited periods predicted by our computations when $X_{\rm He} = 0.80$ ($370 \lesssim \Pi \lesssim 1150$ s) is much wider than the range of periods shown by the star ($380 \lesssim \Pi \lesssim 420$ s). For this case, the three unstable modes with periods close to the observed ones are $\ell = 1$ p mixed modes with $k = 5$ ($\Pi \sim 431$ s), $k = 6$ ($\Pi \sim 398$ s), and $k = 7$ ($\Pi \sim 372$ s)[7]. On the other hand, in the case of the 0.1921 $M_\odot$ models (lower panel), it seems that there is no way to get a range of excited periods compatible with that exhibited by WASP J0247−25B. This is because the excited modes in our models have periods longer than the periods of the star, irrespective of the value that we adopt for $X_{\rm He}$ at the driving region.

From the above analysis, we conclude that the driving region ($\log T \sim 4.7$) of the star WASP J0247−25B must be characterized by a much higher He abundance than that predicted by our pre-WD evolutionary models. The He abundances of pre-WD stars can depend on details of the previous binary evolution, such as different donor star masses of the initial binary system and/or

the beginning of mass loss at different times than considered in our computations. The exploration of these issues is beyond the scope of this paper.

4.3. KIC 9164561

Following the reverse approach than for WASP J0247−25B, here we explore how low the He abundance at the driving region must be as to prevent pulsational instabilities in the nonvariable star KIC 9164561. For a 0.1706 $M_\odot$ pre-WD model at $T_{\rm eff} \sim 10\,400$ K, which is very close to the location of this star in the $T_{\rm eff} - \log g$ plane (see Fig. 1), we found that KIC 9164561 must have $X_{\rm He} \lesssim 0.46$ in order to avoid pulsational excitation. This is $\sim 25\%$ lower than the canonical value predicted by the previous evolution ($X_{\rm He} = 0.584$) for the 0.1706 $M_\odot$ sequence.

5. Summary and conclusions

In this paper, we have presented a detailed linear pulsation stability analysis of pre-WD stars employing the set of state-of-the-art evolutionary models of Althaus et al. (2013). This is the third paper in a series on pulsating low-mass, He-core WDs (including ELM WDs), with the first one focused on the adiabatic properties (Córsico & Althaus 2014a) and the second one devoted to the nonadiabatic pulsation stability features of these stars (Córsico & Althaus 2016). In the present paper, we explore the stability pulsation properties of low-mass He-core stellar models at phases prior to the WD evolution, that is, from effective temperatures ∼6000 K until the stages before the stars reach their maximum effective temperature at the beginning of the first cooling branch. This study was inspired by the discovery of the first two pulsating stars that could be the precursors of pulsating low-mass (including ELM) WDs WASP J0247−25B and WASP J1628+10B (Maxted et al. 2013, 2014). We assess the pulsational stability of radial ($\ell = 0$) and nonradial ($\ell = 1, 2$) g and p modes for stellar models belonging to a set of 11 evolutionary sequences extracted from the computations of Althaus et al. (2013), with masses in the range 0.1554−0.2724 $M_\odot$.

Our main findings are summarized below:

− For stellar models in which element diffusion is neglected, we have confirmed and explored in detail a new instability strip in the domain of low gravities and low effective temperatures of the $T_{\rm eff} - \log g$ diagram, where low-mass pre-WD stars – the precursors of low-mass and ELM WDs – are currently found. The destabilized modes are radial and nonradial p, g, and p-g mixed modes (see Figs. 2−4), excited by the $\kappa - \gamma$ mechanism acting mainly at the He^+-He^{++} partial ionization region ($\log T \sim 4.7$), with non-negligible contributions also from the $He-He^+$ ($\log T \sim 4.42$), and $H-H^+$ ($\log T \sim 4.15$) partial ionization zones at low effective temperatures ($T_{\rm eff} \lesssim 8000-8500$ K, see Fig. 5). Jeffery & Saio (2013) have found pulsation instability of radial modes due to the same driving mechanism, using stellar models completely independent of those employed in this work.
− The nonradial $\ell = 1$ and $\ell = 2$ blue edges of the instability strip, which are almost identical with each other, are hotter and somewhat less steep than the radial ($\ell = 0$) blue edge (see Fig. 1).
− Regarding the ranges of periods of the excited modes, they are strongly dependent on the value of the stellar mass (Figs. 8 and 9). For nonradial dipole modes, the longest excited periods reach values in excess of ∼15 000 s for the highest-mass sequence showing unstable modes

---

[7] We have not made any attempt to fit exactly the observed periods by finely tunning the abundances of He in the driving region, nor considering other harmonic degrees apart from $\ell = 1$.

($M_\star = 0.2026\,M_\odot$), and this limit strongly decreases to ~ 3000 s for the less massive sequence ($M_\star = 0.1554\,M_\odot$) considered. In turn, the shortest excited periods range from ~ 50 s for $M_\star = 0.1554\,M_\odot$, to ~ 3000 s for $M_\star = 0.2026\,M_\odot$. In the case of radial modes, much fewer modes became unstable, with periods in the range $\sim 70-2000$ s for models with $M_\star = 0.1554\,M_\odot$, and $\gtrsim 10\,000$ s for models with $M_\star = 0.1554\,M_\odot$. For high $T_{\rm eff}$, radial modes with $k = 0, 1, 2, 3, 4$ are excited for the sequence with $M_\star = 0.1554\,M_\odot$, whereas for sequences more massive than $0.1822\,M_\odot$, only the fundamental radial ($k = 0$) mode is excited. For lower $T_{\rm eff}$, a modestly larger number of radial modes are excited.

- As for the strength of the pulsational instabilities, generally the most excited modes (that is, with the shortest e-folding times) are those g and p modes experiencing avoided crossings, characterized by short periods ($\tau_{\rm e} \sim 0.01-1$ yr), as can be seen in Fig. 7. In contrast, modes with longer periods are much more weakly destabilized, involving longer e-folding times ($\tau_{\rm e} \sim 10-10^6$ yr), but still much shorter than the evolutionary timescales.

- A direct comparison of our findings with the results of Jeffery & Saio (2013) is not possible because both stability analyses are based on very different stellar models and distinct pulsation codes. We can, however, compare our instability domain (without diffusion, with $0.49 \lesssim X_{\rm He} \lesssim 0.62$) with the set of nonadiabatic models of Jeffery & Saio (2013) in the case in which their envelope models have $X_{\rm He} = 0.48$ ($X_{\rm H} = 0.50$) (see Fig. 10). We found satisfactory agreement, although admittedly, the radial-mode blue edge of Jeffery & Saio (2013) is significantly hotter than ours. In addition, we found far fewer excited radial modes than did Jeffery & Saio (2013).

- When time-dependent element diffusion is taken into account in our models, the instability domain becomes substantially narrower and the blue edge is much cooler than in the case in which diffusion is neglected (see Fig. 11). In this case, by virtue of the driving region at $\log T \sim 4.7$ becoming rapidly depleted in He, the modes are excited mainly by the $\kappa - \gamma$ mechanism acting at the $H-H^+$ partial ionization zone. In view of the narrowness of the effective temperature range in which pulsational instability is found, and because none of the two pre-ELMV stars known to date are accounted for by these computations, we conclude that element diffusion does not occur at these evolutionary stages if the $\kappa - \gamma$ mechanism is responsible for the excitation of the observed pulsations. Processes that might prevent diffusion could include stellar rotation and/or mass loss. This is a very important issue that deserves to be explored in depth.

- Our computations are successful in explaining the location of the pre-ELMV WD star WASP J1628+10B in the $T_{\rm eff} - \log g$ plane (Fig. 1) and also account for the observed range of periods exhibited by this star (Fig. 14). On the other hand, our nonadiabatic models fail to explain the existence of the pre-ELMV WD star WASP J0247−25B. This could indicate that the He abundance in the driving region of this star must be much larger than our evolutionary computations predict, and that the mass of the donor star in the initial binary system could be different from that considered in our computations ($1\,M_\odot$). Alternatively, the pulsations of this star could be due to a different excitation mechanism than the $\kappa - \gamma$ mechanism considered here. In order to explore what the actual He abundance should be to get pulsational instability through the $\kappa - \gamma$ mechanism at the right $T_{\rm eff}$ and $\log g$, with the range of periods displayed by this star, we artificially modify $X_{\rm He}$ at the region of the opacity bump due to the He^+-He^{++} partial ionization zone. We found that the star should have $X_{\rm He} \gtrsim 0.70$ ($X_{\rm H} \lesssim 0.29$) if its effective temperature and gravity are $T_{\rm eff} = 11\,380$ K and $\log g = 4.58$ (Figs. 15). This is in good agreement with the results of Jeffery & Saio (2013).

- The nonvariable pre-ELM WDs considered fall outside our theoretical instability domain, except KIC 916456, which is located well within the predicetd nonradial ($\ell = 1, 2$) instability region (see Fig. 1). We found that, in order to prevent pulsational excitation through the $\kappa - \gamma$ mechanism, the He abundance at the driving zone of this star must be $X_{\rm He} \lesssim 0.46$.

The discovery of two pulsating pre-ELMV WDs reported by Maxted et al. (2013, 2014) indicates the possible existence of a new class of pulsating stars in the late stages of evolution of low-mass WDs. The full exploration of the nonadiabatic properties of stellar models through this domain reported in the present paper, along with the study by Jeffery & Saio (2013), constitute the first solid basis to interpret present and future observations of pulsating pre-ELMV WDs. New discoveries of additional members of this new class of pulsating stars and their analysis in the context of the present theoretical background will allow us to shed light on the evolutionary history of their progenitor stars.

References

Aizenman, M., Smeyers, P., & Weigert, A. 1977, A&A, 58, 41
Althaus, L. G., & Benvenuto, O. G. 2000, MNRAS, 317, 952
Althaus, L. G., Serenelli, A. M., & Benvenuto, O. G. 2001, ApJ, 554, 1110
Althaus, L. G., Serenelli, A. M., Panei, J. A., et al. 2005, A&A, 435, 631
Althaus, L. G., Panei, J. A., Romero, A. D., et al. 2009, A&A, 502, 207
Althaus, L. G., Córsico, A. H., Isern, J., & García-Berro, E. 2010, A&ARv, 18, 471
Althaus, L. G., Miller Bertolami, M. M., & Córsico, A. H. 2013, A&A, 557, A19
Antoci, V., Handler, G., Campante, T. L., et al. 2011, Nature, 477, 570
Antoci, V., Cunha, M., Houdek, G., et al. 2014, ApJ, 796, 118
Bell, K. J., Kepler, S. O., Montgomery, M. H., et al. 2015, in 19th European Workshop on White Dwarfs, eds. P. Dufour, P. Bergeron, & G. Fontaine, ASP Conf. Ser. 493, 217
Bohm, K. H., & Cassinelli, J. 1971, A&A, 12, 21
Böhm-Vitense, E. 1958, Z. Astrophys., 46, 108
Breton, R. P., Rappaport, S. A., van Kerkwijk, M. H., & Carter, J. A. 2012, ApJ, 748, 115
Brickhill, A. J. 1991, MNRAS, 251, 673
Brown, W. R., Kilic, M., Allende Prieto, C., & Kenyon, S. J. 2010, ApJ, 723, 1072
Brown, W. R., Kilic, M., Allende Prieto, C., & Kenyon, S. J. 2012, ApJ, 744, 142
Brown, W. R., Kilic, M., Allende Prieto, C., Gianninas, A., & Kenyon, S. J. 2013, ApJ, 769, 66
Burgers, J. M. 1969, Flow Equations for Composite Gases (New York: Academic Press)
Carter, J. A., Rappaport, S., & Fabrycky, D. 2011, ApJ, 728, 139
Cassisi, S., Potekhin, A. Y., Pietrinferni, A., Catelan, M., & Salaris, M. 2007, ApJ, 661, 1094
Christensen-Dalsgaard, J., & Houdek, G. 2010, Ap&SS, 328, 51
Córsico, A. H., & Althaus, L. G. 2006, A&A, 454, 863
Córsico, A. H., & Althaus, L. G. 2014a, A&A, 569, A106
Córsico, A. H., & Althaus, L. G. 2014b, ApJ, 793, L17
Córsico, A. H., & Althaus, L. G. 2016, A&A, 585, A1

Córsico, A. H., Althaus, L. G., & Miller Bertolami, M. M. 2006, A&A, 458, 259

Córsico, A. H., Romero, A. D., Althaus, L. G., & Hermes, J. J. 2012, A&A, 547, A96

Cox, J. P. 1968, Principles of stellar structure - Vol. 1: Physical principles; Vol. 2: Applications to stars (New-York: Gordon and Breach Science Publisher)

Cox, J. P. 1980, Theory of stellar pulsation (Princeton University Press)

Deheuvels, S., & Michel, E. 2010, Ap&SS, 328, 259

Driebe, T., Schoenberner, D., Bloecker, T., & Herwig, F. 1998, A&A, 339, 123

Fontaine, G., & Brassard, P. 2008, PASP, 120, 1043

Gianninas, A., Dufour, P., Kilic, M., et al. 2014, ApJ, 794, 35

Gianninas, A., Kilic, M., Brown, W. R., Canton, P., & Kenyon, S. J. 2015, ApJ, 812, 167

Haft, M., Raffelt, G., & Weiss, A. 1994, ApJ, 425, 222

Hermes, J. J., Montgomery, M. H., Winget, D. E., et al. 2012, ApJ, 750, L28

Hermes, J. J., Montgomery, M. H., Gianninas, A., et al. 2013a, MNRAS, 436, 3573

Hermes, J. J., Montgomery, M. H., Winget, D. E., et al. 2013b, ApJ, 765, 102

Iglesias, C. A., & Rogers, F. J. 1996, ApJ, 464, 943

Istrate, A. G., Tauris, T. M., & Langer, N. 2014, A&A, 571, A45

Itoh, N., Hayashi, H., Nishikawa, A., & Kohyama, Y. 1996, ApJS, 102, 411

Jeffery, C. S., & Saio, H. 2013, MNRAS, 435, 885

Kawaler, S. D. 1993, ApJ, 404, 294

Kepler, S. O., Kleinman, S. J., Nitta, A., et al. 2007, MNRAS, 375, 1315

Kepler, S. O., Pelisoli, I., Koester, D., et al. 2015, MNRAS, 446, 4078

Kilic, M., Brown, W. R., Allende Prieto, C., et al. 2011, ApJ, 727, 3

Kilic, M., Brown, W. R., Allende Prieto, C., et al. 2012, ApJ, 751, 141

Kilic, M., Hermes, J. J., Gianninas, A., & Brown, W. R. 2015, MNRAS, 446, L26

Kleinman, S. J., Kepler, S. O., Koester, D., et al. 2013, ApJS, 204, 5

Koester, D., Voss, B., Napiwotzki, R., et al. 2009, A&A, 505, 441

Lee, U., & Bradley, P. A. 1993, ApJ, 418, 855

Magni, G., & Mazzitelli, I. 1979, A&A, 72, 134

Maxted, P. F. L., Anderson, D. R., Burleigh, M. R., et al. 2011, MNRAS, 418, 1156

Maxted, P. F. L., Serenelli, A. M., Miglio, A., et al. 2013, Nature, 498, 463

Maxted, P. F. L., Serenelli, A. M., Marsh, T. R., et al. 2014, MNRAS, 444, 208

Osaki, J. 1975, PASJ, 27, 237

Panei, J. A., Althaus, L. G., Chen, X., & Han, Z. 2007, MNRAS, 382, 779

Rappaport, S., Nelson, L., Levine, A., et al. 2015, ApJ, 803, 82

Saio, H. 2013, in EPJ Web Conf., 43, 5005

Saio, H., Winget, D. E., & Robinson, E. L. 1983, ApJ, 265, 982

Sarna, M. J., Ergma, E., & Gerškevitš-Antipova, J. 2000, MNRAS, 316, 84

Scuflaire, R. 1974, A&A, 36, 107

Steinfadt, J. D. R., Bildsten, L., & Arras, P. 2010, ApJ, 718, 441

Strittmatter, P. A., & Wickramasinghe, D. T. 1971, MNRAS, 152, 47

Tassoul, M., Fontaine, G., & Winget, D. E. 1990, ApJS, 72, 335

Tremblay, P.-E., Bergeron, P., & Gianninas, A. 2011, ApJ, 730, 128

Unglaub, K., & Bues, I. 2000, A&A, 359, 1042

Unno, W., Osaki, Y., Ando, H., Saio, H., & Shibahashi, H. 1989, Nonradial oscillations of stars, 2nd edn. (Tokyo: T. University of Tokyo Press)

Van Grootel, V., Fontaine, G., Brassard, P., & Dupret, M.-A. 2013, ApJ, 762, 57

van Kerkwijk, M. H., Rappaport, S. A., Breton, R. P., et al. 2010, ApJ, 715, 51

Winget, D. E., & Kepler, S. O. 2008, ARA&A, 46, 157